Additive Manufacturing Letters 15 (2025) 100345

Contents lists available at ScienceDirect

Additive Manufacturing Letters

journal homepage: www.elsevier.com/locate/addlet

Short Communication

Multi-scale mechanical characterization of an additively manufactured Fe-based glass-forming alloy

C. Garrote-Junco [a,b], A. Ghavimi [c], R. Busch [c], M.T. Pérez-Prado [a], M. Rodríguez-Sánchez [a,d,*]

[a] IMDEA Materials Institute, Calle Eric Kandel, 2 Getafe, 28906 Madrid, Spain
[b] Escuela Técnica Superior de Ingeniería Aeronáutica y del Espacio, Universidad Politécnica de Madrid, Pl. del Cardenal Cisneros, 3, Moncloa - Aravaca, 28040 Madrid, Spain
[c] Saarland University, Institute of Metallic Materials, Campus C6.3 66123, Saarbrücken, Germany
[d] Materials Science and Engineering Department, Universidad Carlos III de Madrid, Av. De la Universidad 30, Leganés, 28911 Madrid, Spain

ARTICLE INFO

Keywords:
Kuamet 6B2
Laser powder bed fusion
Mechanical properties
Fe-based metallic glasses
Defect structure

ABSTRACT

This work aims to investigate the influence of specimen size and loading direction on the mechanical response of a laser-powder-bed-fused (LPBF) Fe-based metallic glass (Kuamet 6B2). Cuboidal specimens of sizes ranging from 4 to 8 mm were fabricated and then systematically characterized by a range of complementary techniques including optical microscopy, image analysis, differential scanning calorimetry and electron backscattered diffraction (EBSD). All builds exhibited three highly oriented defect families: elongated lack-of-fusion pores perpendicular to BD, oblique internal cracks and large surface cracks normal to BD. These defects, along with limited amorphous retention, dominate the bulk compliance and strength.

The mechanical behavior was assessed by room temperature uniaxial compression, both parallel and perpendicular to the build direction (BD), as well as by nanoindentation. A clear, direction-dependent size effect emerges. Under loading parallel to BD, strength and uniform strain diminish with increasing specimen size, consistent with defect closure and the correlation between density and mechanical response. In contrast, when loading is perpendicular to BD, strength and uniform strain increase with size, due to the reduction of normalized defect length scales relative to specimen width. The ensuing drop in stress-intensity at defect tips, suppressing crack propagation. Nanoindentation on defect-free regions revealed substantially higher local stiffness than bulk values, underscoring that the macroscopic response is defect-controlled rather than matrix-controlled.

1. Introduction

Metallic Glasses (MGs), also termed amorphous metals, are a family of alloys which can retain an amorphous structure lacking long-range atomic order when they are cooled at high rates (commonly higher than 10^5 K/s) from the molten state [1–3]. The absence of grain boundaries, secondary phases, or atomic defects such as dislocations in such amorphous structure endows these materials with properties distinct from crystalline counterparts [4–6]. Fe-based MGs, for instance, possess soft magnetic properties such as low coercivity and relatively high saturation magnetization, high electrical resistivity, and high magnetic permeability [7–10], making them promising to reduce energy losses in rotors and stators of electrical machines [11]. However, conventional manufacturing routes rarely achieve the cooling rates required to retain a high fraction of amorphous phase in bulk components, i.e. those with dimensions exceeding 1 mm [6–8].

Laser powder bed fusion (LPBF) can reach local cooling rates as high as 10^7 K/s [12–15] and recent works have shown promising results when producing large parts from Fe-based MG compositions with high relative density using specific combinations of processing parameters and scanning strategy [16,17]. However, due to the limited glass forming ability (GFA) of these alloys, especially of those that are more relevant for sustainable applications as they do not contain rare earths, Co, or P [10], the combinations of parameters that yield high density tend to induce crystallization during subsequent thermal cycles, which severely hinders magnetic performance [18]. On the other hand, processing parameters can be selected to maximize the amorphous fraction of the part, which improves the magnetic properties, but generates internal defects such as porosity and cracks, weakening the material mechanically [19–21].

* Corresponding author.
E-mail address: marcos.rodriguez@imdea.org (M. Rodríguez-Sánchez).

https://doi.org/10.1016/j.addlet.2025.100345
Received 15 October 2025; Received in revised form 19 November 2025; Accepted 27 November 2025
Available online 28 November 2025

Kuamet 6B2 is a commercial Fe-based glass-forming composition with relatively low coercivity (6 A/m) and high saturation magnetization (145 Am^2/kg) in the fully amorphous state. This alloy's critical casting thickness, a commonly used indicator to describe the GFA, is as low as 120 μm, and thus to date it has not been possible to optimize simultaneously the density and the amorphous fraction in LPBF-manufactured samples. Earlier works on LPBF-manufactured Kuamet 6B2 report the presence of internal defects such as voids and cracks, as well as the coexistence of (nano)crystalline and amorphous phases, for a wide range of processing conditions and scanning strategies [18,22–27]. To date, most studies on Kuamet 6B2 fabricated by additive manufacturing have focused on characterizing the magnetic properties [18,22–27], which are of primary interest for industrial applications. However, the macro- and micromechanical behavior, which is also relevant for applications as structural stability is also required during operation, remains underexplored. In particular, the effect of persistent highly oriented defects on the micromechanical behavior of LPBF-processed samples, as well as the size effects must be understood. Furthermore, the mechanical properties at the microscale have not been studied on this alloy, where the range of microstructural features previously reported [18,27] is expected to yield heterogeneous micromechanical properties. A deeper understanding of the interplay between said internal defects, microstructure, and mechanical properties is essential for the successful adoption of this material in highly efficient next-generation electrical machines.

This work aims to contribute to filling this gap in the understanding of the LPBF-processed Kuamet 6B2 alloy by presenting the first investigation on the effect of the defect structure and of the (micro)structure on the multi-scale mechanical performance of specimens of different sizes. With that goal, a combined macro- and micromechanical testing campaign was put in place, and the results are related to the presence of voids, cracks and (micro)structural features in the manufactured samples.

2. Materials and methods

2.1. Laser powder bed fusion

The Kuamet 6B2 ($Fe_{73.7}B_{11}Si_{11}Cr_{2.3}C_2$ [at. %]) feedstock powder was provided by EPSON Atmix Japan. The powder was atomized via a spinning water atomization process (SWAP) [28] and was later handled inside a glovebox with an inert Ar atmosphere to prevent oxidation. The particle size distribution, measured using a Bettersize laser particle size analyzer, is characterized by D_{10}, D_{50}, and D_{90} values of 10, 28, and 57 μm, respectively.

The LPBF system used in this study was a Renishaw AM400 furnished with a reduced build volume platform. This system uses a Yb fiber laser with pulsed wave (PW) emission and a beam diameter of 62 μm. An Ar atmosphere was maintained through the process, keeping an O target below 1000 ppm. A meander scanning strategy with a 67° rotation between successive layers was applied. Previous work [18,27] has shown that, with such a simple scanning strategy LPBF processing parameters that promote high relative density tend to induce crystallization, whereas those that favor retention of the amorphous phase typically increase the number of internal defects. For the present study, a combination of parameters previously shown [18] to yield a relatively high density (88 % in 8 × 8 × 9.5 mm^3 prisms) was selected to ensure sufficient mechanical stability for testing. In the same study, these parameters were also found to cause severe devitrification, resulting in an amorphous fraction of only 11 % in the cuboids [18]. In particular, specimens were processed with a laser power (P) of 40 W, a layer thickness (t) of 30 μm, a hatch distance (h) of 80 μm, an exposure time (t_{ON}) of 220 μs, and a point distance (p_d) of 80 μm, which yielded approximately a scan speed (v) of 363 mm/s according to the following formula $v = \frac{pd}{t_{ON}+10}$. The value of 10 in the denominator represents the 10 μs needed for the laser to move from one exposure point to the next under PW mode. Cuboidal specimens with nominal side lengths (S) of 4, 6, and 8 mm were thus manufactured. The actual edge lengths, measured with a caliper after fabrication, averaged 4.17 mm, 6.13 mm, and 8.09 mm, respectively. In total, 30 cuboids were produced, with 10 specimens of each size. Out of these, 2 of each size were reserved for defect and microstructural analysis, while the remaining 8 were used for uniaxial compression tests along two perpendicular loading directions.

2.2. Defect and micro-texture characterization

The relative density of the Kuamet 6B2 LPBF-manufactured samples was first measured via the Archimedes method using a BEL Engineering density kit. For each size, at least two samples were manually ground with grit 320 SiC paper, to avoid surface roughness effects during testing, and the reported values correspond to the average of three measurements per sample. The relative density was also estimated by image analysis from optical micrographs of cross-sections parallel to BD using an Olympus BX51 microscope and the image analysis ImageJ/Fiji software [29]. To avoid surface effects, all images were cropped with the largest rectangle that could fit within the irregular edges. The use of the Weka trainable segmentation package [30] enabled segmentation of the optical micrographs into three different classes: bulk material, voids, and cracks. The morphology of the voids was analyzed using Fiji's 'Analyze Particles' plug-in. Two types of cracks were observed: internal cracks, tilted at an angle with respect to the BD and surface cracks growing mostly perpendicular to BD. Internal cracks were also characterized with Fiji's 'Analyze Particles' plug-in, and their maximum caliper (i.e. the longest distance between any two points along the crack) was recorded. The inclination of internal cracks with respect to the BD was measured with Fiji's 'Directionality' plug-in. The mean length of surface cracks could not be obtained from segmented images and was calculated by averaging manual measurements of at least ten cracks for each specimen with Fiji's 'straight segment' tool. Sample preparation for optical microscopy examination consisted of sectioning using a Struers Secotom 20 disc cutting machine, followed by surface grinding with SiC paper of grit sizes 320, 600, 1200, 2400 and final mirror polishing using diamond pastes with particle sizes from 9 to 1 μm.

The amorphous fraction (AM %) was measured by differential scanning calorimetry (DSC) using a Perkin Elmer DSC8000. A piece of approximately 3 × 3 × 1 mm^3 was cut from a printed specimen of each size and a constant heating rate of 20 K/min was applied. AM % was calculated as the ratio between the crystallization enthalpy of the samples and that of a fully amorphous melt-spun ribbon of the same composition ($AM\ \% = \Delta H_{cr,sample}/\Delta H_{cr,ribbon}$). As expected, it was found that AM % was relatively low in all the LPBF manufactured cuboids. Average fractions of 10 %, 14 %, and 8 % were estimated for 4-, 6-, and 8-mm sized specimens, with $a \pm 5$ % error due to possible deviations in the calculation of $\Delta H_{cr,sample}$ from DSC curves.

Microtexture analysis was carried out using a using a FEI Helios NanoLab 600i FEG-SEM electron backscatter diffraction (EBSD) system equipped with an Oxford Instruments detector and with the Aztec data acquisition and analysis software package. Measurements were conducted using a working distance of 8 mm, an acceleration voltage of 20 kV, a current of 2.7 nA, and a step size of 120 nm.

2.3. Mechanical testing

The mechanical behavior of the cubic LPBF manufactured samples with nominal edge dimensions of 4, 6, and 8 mm were studied using a combined macro- and micromechanical approach. Macromechanical testing yields the 3D response of the material accounting for the coupled contribution of the internal defect structure and the (micro)structure, while micromechanical testing allows to probe the local response of defect-free regions and thus to isolate the contribution of the (micro) structure.

Room temperature uniaxial compression tests were conducted both parallel and perpendicular to the build direction (BD) in an Instron 3384 electromechanical system furnished with a 150 kN load cell at room temperature. Samples were placed between two plates that moved at a constant crosshead speed equivalent to an initial strain rate of 5 $*10^{-4}s^{-1}$. A minimum of three tests were performed for each testing condition. The displacement of the load plates was measured using an Instron dynamic extensometer with 12.5 mm gauge length and ±2.5 mm travel. The Young's modulus (E), the maximum stress (σ_{max}) and the uniform strain (e_u) were recorded for each testing condition. Fracture surfaces were imaged using an Apreo 2S (ThermoFisher Scientific) FEGSEM at a 10 mm working distance, 20 kV accelerating voltage and 0.4 nA beam current. For macromechanical testing, the cuboidal specimens were ground with 600-grit SiC paper to ensure parallel loading surfaces.

Micromechanical nanoindentation tests were carried out on an 8-mm cuboid specimen. The sample was ground and polished to ensure the test surface was parallel to the base and free of visible scratches. An area of 120 × 70 μm was indented with a Hynstron Triboindenter TI 950 using a step size of 1.2 μm and a maximum load of 5 mN. The reduced modulus (E_r), measured by the instrument, was converted to E using the following formula:

$$E = \left(1-\nu^2\right)\left(\frac{1}{E_r} - \frac{1-\nu_i^2}{E_i}\right)^{-1}$$

where ν is the material's Poisson ratio (approximately 0.28) and E_i and ν_i are the elastic modulus and Poisson's ratio of the instrument, respectively. Three cyclic load tests were performed, and the instrument compliance was adjusted to ensure that the measured hardness and reduced modulus remained constant across all load cycles. Following this calibration step, values for E_i and ν_i were found to be 1141 GPa and 0.07, respectively.

3. Results and discussion

3.1. Density and analysis of the defect structure

Fig. 1 illustrates the variation of the density, measured by the Archimedes method, with size (S) for all the LPBF manufactured cuboids. Despite the relatively wide scatter in the data, this figure reveals that there is a decrease in density with increasing S. The average density in the printed samples amounted to 6.99 g/cm^3 (4 mm), 6.96 g/cm^3 (6 mm), and 6.89 g/cm^3 (8 mm). These values are naturally lower than the density of a cast Kuamet 6B2 sample (7.14 g/cm^3). Consistently, estimation of the relative area density from optical micrographs by image analysis yielded values of 92.41 %, 90.63 %, and 90.92 % for 4-, 6-, and 8-mm cuboids, respectively. The average density data are summarized in Table 1.

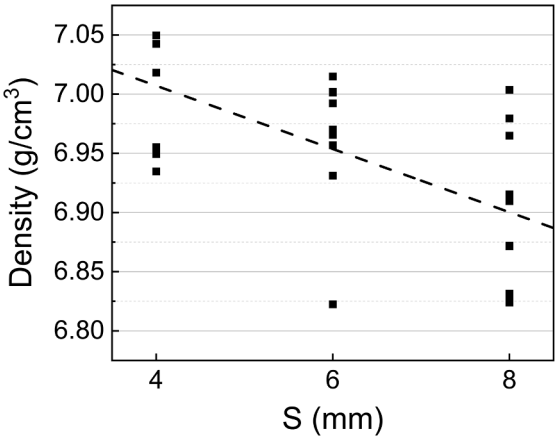

Fig. 1. Archimedes density with respect to sample size (S).

Irrespective of their size, all LPBF-manufactured cuboids exhibited the same three types of defects: voids, internal cracks, and surface cracks. Fig. 2a shows a representative optical micrograph of a cross section parallel to BD of an 8-mm cuboid, where the three types of defects are isolated (see insets 1, 2, and 3, respectively). The porosity observed in all samples corresponds to lack-of-fusion (LoF) defects, which is known to arise from insufficient input energy to fully melt the feedstock powder and typically appear as elongated pores oriented perpendicular to the BD [31]. The total fraction of voids was calculated including those with areas larger than 2500 pixels. Such voids, named hereafter "type-1 voids", are highlighted in black as an example in region (1) of Fig. 2a. The area fraction of type-1 voids in cuboids with 4-, 6-, and 8-mm sides amount to 5.01 %, 7.80 %, and 7.48 %, respectively (Table 1). The observed reduction of the area fraction of LoF voids as the sample's cross section decreases is attributed to the smaller associated rescan times. Indeed, shorter hatch tracks lead to an increase in the basal temperature of the material which leads to higher temperatures during the heating cycles of newly scanned tracks [32–35]. Such heat accumulation within the sample can consequently enhance fusion between powder particles, ultimately yielding denser parts [36]. The average type-1 void length (a_1, measured perpendicularly to BD), width (b_1, measured in parallel to BD) and the aspect ratio (a_1/b_1) are summarized in Table 1 and the variation a_1 with respect to the sample size is represented in Fig. 2b A minor increase in a_1 is noted when the specimen size increases from 4 mm to 6 and 8 mm. Specifically, a_1 increases from 145 μm to 170 μm and 162 μm, respectively. Moreover, all samples show type-1 voids which are mainly elongated in the perpendicular direction to BD ($a_1 > b_1$).

Since it is expected that the largest pores are preferential crack initiation sites [37] and that they are likely to have a dominant influence on the mechanical response, a subset of type-1 voids with areas larger than 20,000 pixels was isolated. Such voids, hereafter termed as type 2, are highlighted in region (1) of Fig. 2a and their main characteristics (area fraction, length (a_2), width (b_2), and aspect ratio (a_2/b_2)) are summarized in Table 1. The area corresponding to type-2 voids also increases with increasing specimen size, from 2.29 % in 4 mm cuboids to 4.95 % and 4.45 % in 6- and 8-mm cuboids, respectively. Fig. 2b illustrates the variation of a_2 with specimen size. It can be seen that a_2 increases from 279 μm (4 mm) to 351 μm (6 mm), and 344 μm (8 mm),

Table 1
Summary of the density and defect characteristics for the three sample sizes studied.

		4 mm	6 mm	8 mm
Arquimedes density (g/cm^3)		6.99	6.96	6.89
Relative area density (from OM) (%)		92.41	90.63	90.92
Type-1 voids > 2500 pixels	Number (-)	51	141	267
	Area fraction (%)	4.30	7.07	6.63
	Avg. a_1 (μm)	145	170	162
	Avg. b_1 (μm)	127	138	136
	Avg. a_1/b_1 (-)	1.14	1.23	1.19
	Avg. a_1/S (-)	0.035	0.027	0.020
Type-2 voids > 20,000 pixels	Number (-)	11	36	62
	Area fraction (%)	2.29	4.95	4.45
	Avg. a_2 (μm)	279	351	344
	Avg. b_2 (μm)	201	237	250
	Avg. a_2/b_2 (-)	1.38	1.48	1.37
	Avg. a_2/S (-)	0.067	0.057	0.043
Internal cracks	Number (-)	6040	3458	1237
	Area fraction (%)	2.59	1.57	1.60
	Avg. a_3 (μm)	45	29	31
	Avg. a_3/S (-)	0.011	0.005	0.004
Surface cracks	Number (-)	10	21	26
	Area fraction (%)	N/A	N/A	N/A
	Avg. a_4 (μm)	318	321	306
	Avg. a_4/S (-)	0.076	0.052	0.038

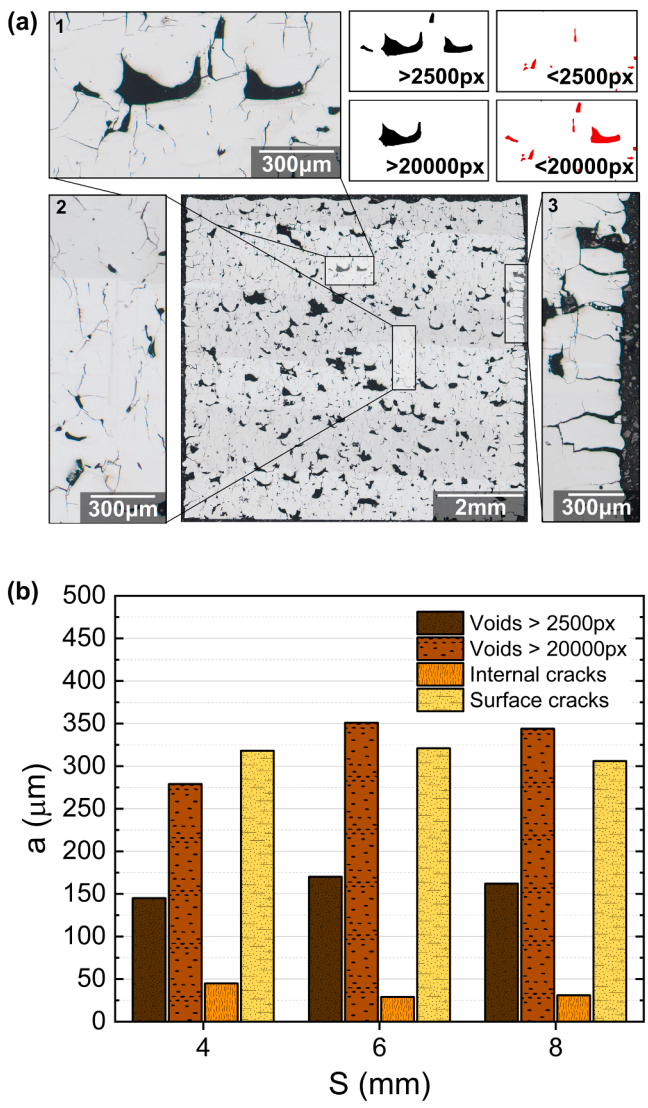

Fig. 2. (a) Optical micrograph of a cross section parallel to BD of an 8 mm sample. The insets highlight the different classes of defects: (1) lack of fusion pores, (2) internal cracks, and (3) surface cracks. (b) Variation of the defect length (a_i) with respect to the sample size (S).

respectively. The aspect ratio of type 2 voids is larger than that of type-1 voids, indicating a more pronounced elongation perpendicularly to the BD.

Internal and surface cracks have been observed in additively manufactured Fe-based metallic glass parts [19,38,39]. These defects are formed as a result of the thermal stresses originated from the solidification of consecutive tracks and/or layers [19], which cannot be sustained by brittle materials with high sensitivity to temperature gradients [38,39]. Table 1 summarizes the area fraction and the average length (a_3) of internal cracks. Internal cracks are homogeneously distributed throughout the sample interior, and their area fraction is significantly higher in the 4 mm samples than in larger cuboids (2.59 % (4 mm) vs. 1.57 % (6 mm), and 1.60 % (8 mm), respectively. As shown in Fig. 2b, internal cracks are longest in the 4 mm sample (45 μm) and virtually equally long in the 6 mm and 8 mm specimens (31 and 29 μm, respectively). These cracks are preferentially tilted at 0°, ±5°, ±15°, ±20°, ±25°, ±45° ±50°, ±70°, ±75°, ±85°, and ±90° angles with respect to BD, consistent with previous observations for Kuamet 6B2 [18].

Finally, surface cracks were observed to propagate perpendicular to BD, extending into the interior of the manufactured samples. The average crack length (a_4) is summarized in Table 1 and plotted in Fig. 2b as a function of specimen size. The measured values were 318 μm, 321 μm, and 306 μm for the 4-, 6-, and 8-mm cuboids, respectively, indicating a slightly smaller average length in the largest specimens. The area fraction of surface cracks was not quantified due to the irregularity of the sample surfaces, which prevented an accurate image analysis.

3.2. Macromechanical behavior

Figs. 3a-c illustrate the room temperature engineering stress-strain curves corresponding to the LPBF-manufactured 4-, 6-, and 8-mm cuboids. For each specimen size, tests performed with the compression axis parallel to BD (‖BD, black lines) and perpendicular to BD (⊥BD, red lines) are compared. Three tests were performed for each condition. Irrespective of the specimen size, failure occurs at strains approximately equal or smaller than 2 %. Figs. 3d and 3e illustrate the fracture surface of a representative 6 mm ‖BD specimen, which exhibits typical features of brittle failures in MGs, including shear bands (highlighted with yellow arrows) and smooth facets [40,41].

Fig. 4 summarizes the variation of E, σ_{max} and e_u with the sample size. Fig. 4a shows that there is no perceptible relationship between the sample size and the Young's modulus. However, the average value of Young's Modulus for ‖BD samples is smaller than that of BD samples (33 GPa and 44 GPa, respectively). It is well known that the presence of significant fractions of defects has a notable influence on E. For instance, porosity values between 3 % and 7 % have been reported to reduce E by 16 %, following a negative exponential law, when LPBF-processed the AMZ4 alloy, a widely studied metallic glass composition, was tested under tension [42]. Furthermore, in numerical studies [43], crack densities of 1.5 % have been reported to decrease the Young's modulus by up to 70 %. In the present study, results of image analysis indicated that samples' porosity due to type-1 voids ranges between 4.3 % and 7.1 % and crack density ranged between 1.6 % and 2.6 %. Moreover, type-1 and type-2 voids are elongated perpendicular to the BD, which increases compliance along the BD and is consistent with the lower Young's modulus measured in samples tested parallel to the BD.

Figs. 4b and 4c evidence that the maximum stress and the uniform deformation exhibit opposite trends with sample size for the two investigated loading directions. In the ‖BD samples, both σ_{max} and e_u decrease as the sample size increases, while in ⊥BD samples, σ_{max} and e_u increase with increasing sample size. In particular, as the specimen size increases from 4 mm to 8 mm, σ_{max} in ‖BD samples decreases from 660 to 400 MPa (8 mm), while in ⊥BD samples it increases from 520 to 780 MPa. Conversely, for the same range of specimen sizes, e_u in ‖BD samples decreases from 2.0 to 1.4 % and in ⊥BD samples it increases slightly from 1.5 to 1.6 %.

In the following we correlate the variations in the maximum stress reported in Fig. 4b with the defect structure described in Section 3.1. Internal cracks will not be considered in this analysis because, as shown in Table 1 and Fig. 2, their area fraction is significantly smaller than that of type 1 (and even type 2) voids and their average length is considerably shorter than that of type 2 voids and surface cracks. Therefore, they are not expected to exert a dominant influence on the mechanical behavior.

Fig. 5 schematically illustrates the orientation of type 2 voids (Fig. 5a) and surface cracks (Fig. 5b) with respect to the loading axis for both ‖BD and ⊥BD specimens. Under ‖BD loading, the compression axis is perpendicular to the longer dimension of these two types of defects, which therefore tend to close or decrease in width during testing. This leads to denser specimens in which strength scales with density, which itself increases with decreasing sample size (Fig. 1 and Table 1). In contrast, under ⊥BD loading the compression axis is parallel to the longer dimension of voids and surface cracks, promoting stress localization at pore and crack tips. The supplementary material further elaborates on the three-dimensional stress state of the specimens and the stress intensity factor (SIF) at the tip of an elongated pore or crack. The SIF is proportional to the corresponding a_1/S ratio [44,45], which is

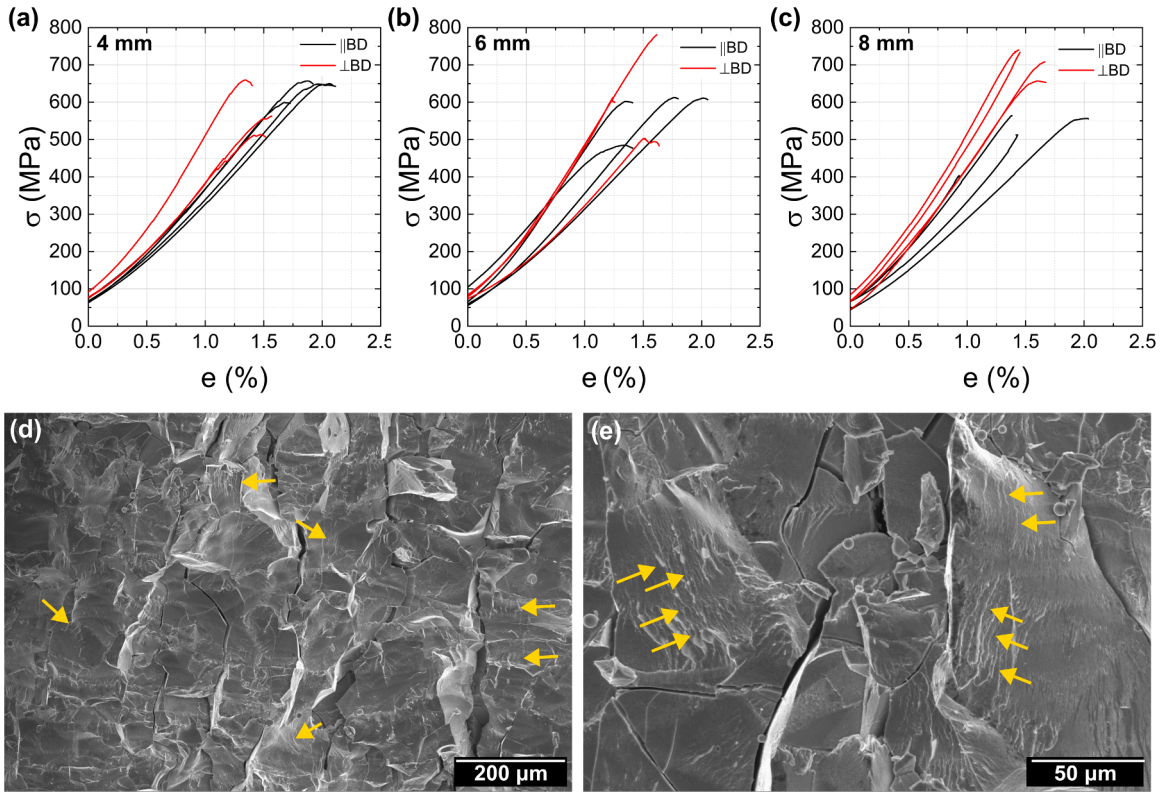

Fig. 3. (a-c) Uniaxial compression engineering stress-strain curves corresponding to 4-, 6-, and 8-mm cuboids. The black curves correspond to tests performed with the compression axis parallel to BD (||BD) and the red curves correspond to tests conducted with the compression axis perpendicular to BD (⊥BD). (d,e) Representative SEM images of the fractured surface of a 6 mm sample tested along the BD. Yellow arrows are used to mark the appearance of shear bands.

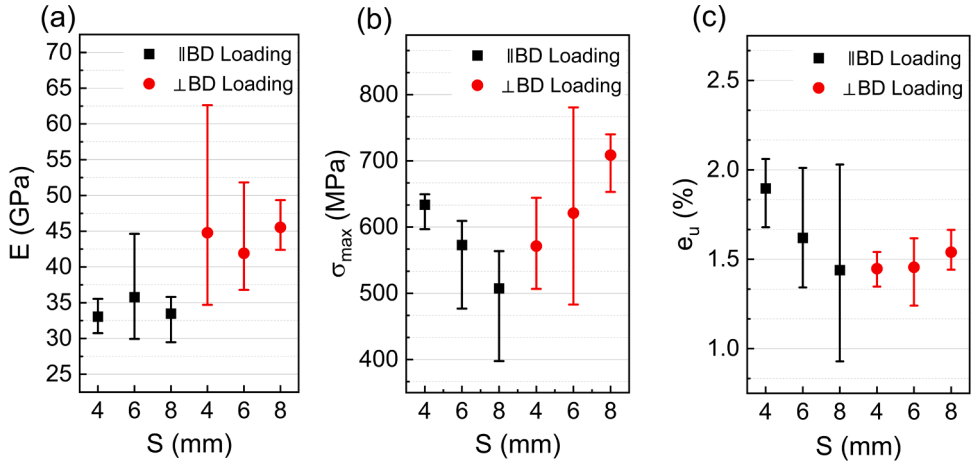

Fig. 4. Variation of (a) the Young's modulus, (b) the maximum stress, and (c) the uniform deformation with respect to the sample size (S) and to the compression loading mode.

reported in Table 1 for voids and surface cracks. Type-2 voids exhibit a_2/S ratios of 0.067, 0.057, and 0.043 in cuboids with 4-, 6-, and 8-mm sides respectively. In turn, surface cracks exhibit a_4/S ratios of 0.076, 0.052, and 0.038, respectively. In both cases the a_i/S ratios decrease with increasing sample size, leading to a lower SIF, suppression of crack propagation and, consequently, higher σ_{max} and e_u.

3.3. Micromechanical behavior

Fig. 6 depicts the local (micro)structure and the corresponding variation of the Young's modulus and of the microhardness in an area free of defects in a representative 8 mm Kuamet 6B2 cuboid. Fig. 6a presents an EBSD band contrast map where gray areas denote crystalline regions and black areas correspond to regions containing amorphous phase or crystallites with sizes that are below the resolution of the measurement (approximately 240 nm). Fig. 6b illustrates an inverse pole figure (IPF) map in the BD, where the orientations of crystallites are colored according to the color key included in the inset. In agreement with earlier studies [18,27,46] both maps confirm that crystallites are mostly present in the heat affected zone (HAZ) surrounding the melt pools (MP), have a random crystallographic texture, and grain sizes that decrease gradually with the distance to the MP. In an earlier study on Kuamet6B2 manufactured under similar conditions [18], it was found that most crystallites were Fe(Si) intermetallics, with a minor fraction of

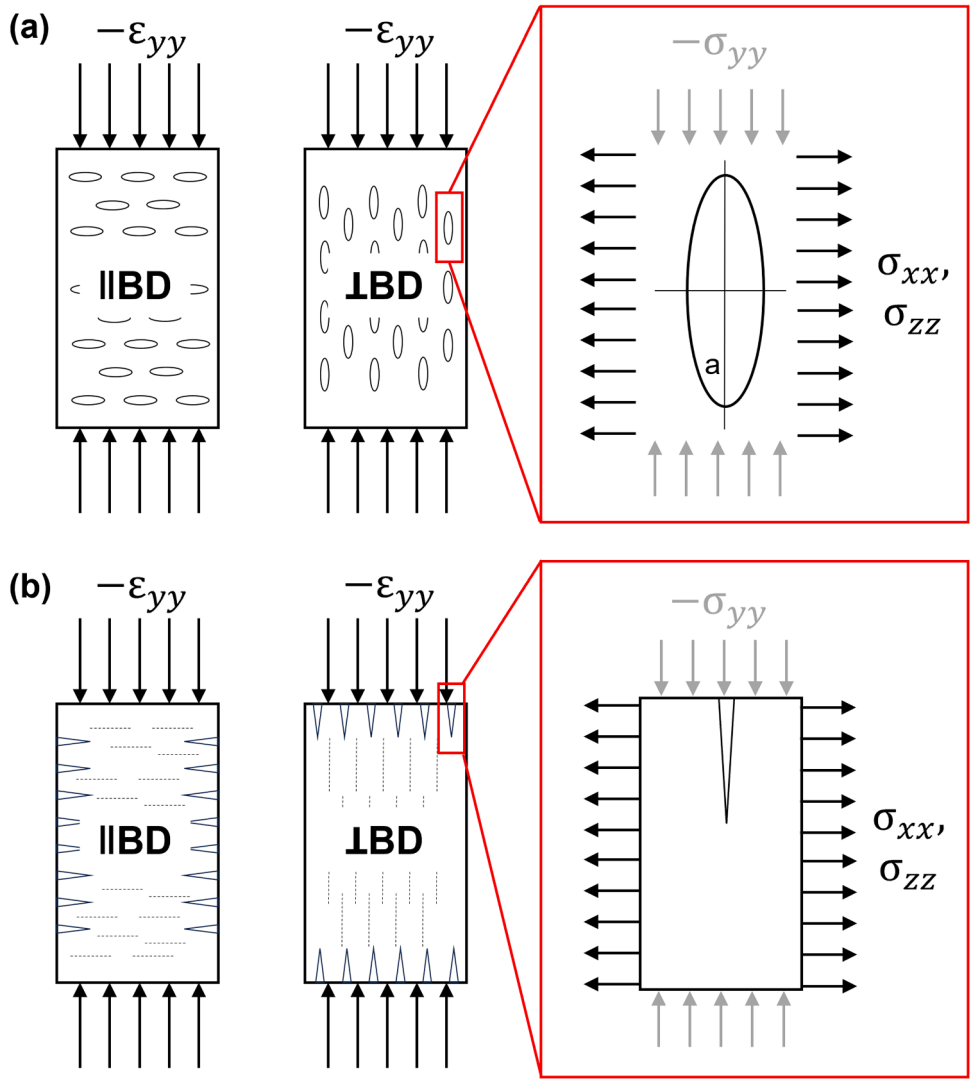

Fig. 5. Schematic illustrating the stress state and the orientation of (a) voids and (b) surface cracks for tests where the compression axis lies parallel (∥BD) and perpendicular (⊥BD) to BD.

Fe borides. Figs. 6c and 6d depict the corresponding Young's modulus and nanohardness (H) maps. Amorphous regions exhibit the lowest Young's modulus and the lowest hardness, with E values ranging between approximately 190 and 220 GPa and hardness value between 11 and 12.5 GPa. The crystalline regions are characterized by a higher Young's modulus, ranging between 230 and 290 GPa, and a higher hardness, comprised between 13 and 16 GPa. The variations in E and H in the crystalline regions are likely attributed to differences in the Fe(Si) grain size and to the heterogeneous spatial distributions of Fe_2B and $Fe_{23}B_6$ [47,48]. While grain size differences and phase spatial arrangement clearly influence micro-mechanical properties, it must be noted that the Young's modulus measured by nanoindentation is as much as 6 times higher than the bulk value measured from the macromechanical compression tests (Fig. 4a). Such large deviation is attributed to the presence of defects, which leads to a significantly higher compliance.

4. Conclusions

In summary, a significant fraction of highly oriented defects was found on Kuamet 6B2 specimens of different sizes processed by laser powder bed fusion. These results are consistent with previous work on the same alloy [18,23,27]. Regardless of the processing parameters or scanning strategy, internal defects and local devitrification have never been fully avoided on Kuamet 6B2. More importantly, the consequences of such defects and crystalline features on the mechanical response of the material had not been thoroughly studied in this composition. The present work provides an understanding of the effect of typically observed voids, cracks and crystallites resulting from devitrification of the previously deposited amorphous layers on the mechanical properties at different length scales. However, it is expected that the complexity of said relationships will increase for intricate print geometries. Hence, future work in the field should aim to eliminate the aforementioned undesired features by means of alloy design or through advanced LPBF processing control. Until then, the following findings must be considered during the design and production of Kuamet 6B2 components using LPBF:

- Irrespective of the sample size, three main kinds of highly oriented defects were identified in the Kuamet 6B2 LPBF manufactured samples: large LoF pores elongated perpendicularly to the BD, oblique internal cracks preferentially propagated at specific angles relative to the BD, and large surface cracks perpendicular to the BD. The presence of these defects has a strong influence on the mechanical behavior.
- The Young's modulus of the LPBF manufactured samples is as much as six times smaller than that of the bulk alloy due to the presence of

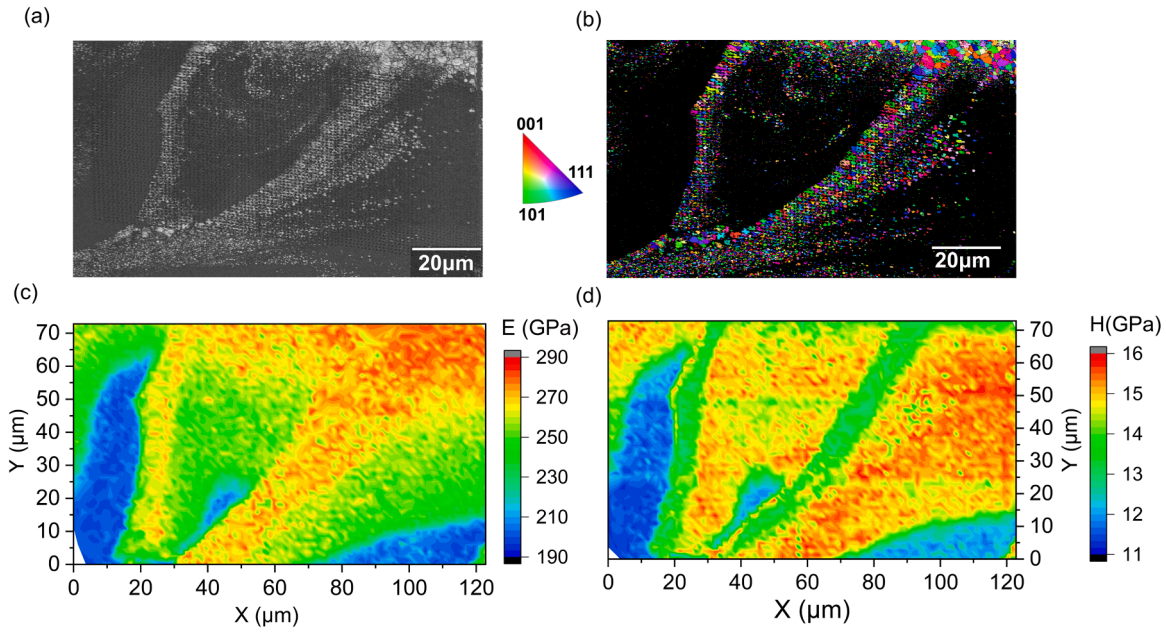

Fig. 6. Local (micro)structure and nanoindentation data corresponding to a representative 8 mm Kuamet 6B2 cuboid processed by LPBF. (a) EBSD band contrast map. Crystalline and amorphous regions are colored in gray and black, respectively; (b) EBSD IPF map in the BD; (c) Young's modulus map; (d) hardness map.

voids and cracks. Moreover, E is smaller when testing parallel to BD than when testing along a direction perpendicular to BD, as in the former case voids and surface cracks tend to close during testing, thus enhancing compliance.

- When testing ∥BD, the maximum stress and uniform deformation exhibit an inverse correlation with sample size. This trend is attributed to the higher density achieved in smaller specimens.
- When testing ⊥BD, the maximum stress and uniform deformation exhibit a positive correlation with sample size. This behavior is attributed to the decrease in the a_i/S ratios, and consequently in the stress intensity factor, with increasing size, which enhances the suppression of crack propagation.

CRediT authorship contribution statement

C. Garrote-Junco: Writing – original draft, Validation, Software, Investigation. **A. Ghavimi:** Writing – review & editing, Investigation. **R. Busch:** Writing – review & editing, Supervision, Project administration, Funding acquisition. **M.T. Pérez-Prado:** Writing – review & editing, Supervision, Funding acquisition, Conceptualization. **M. Rodríguez-Sánchez:** Writing – review & editing, Visualization, Validation, Supervision, Methodology, Formal analysis, Conceptualization.

Declaration of competing interest

The authors declare that they have no known competing financial interests or personal relationships that could have appeared to influence the work reported in this paper.

Acknowledgments

The work hereby presented has been carried out under the scope AM2SoftMag project (GA number 101046870), funded by the European Union. Views and opinions expressed are however those of the author(s) only and do not necessarily reflect those of the European Union or the European Innovation Council and SMEs Executive Agency (EISMEA). Neither the European Union nor the granting authority can be held responsible for them. Extended acknowledgement is given to Miguel Monclús for his assistance with nanoindentation measurements.

Supplementary materials

Supplementary material associated with this article can be found, in the online version, at doi:10.1016/j.addlet.2025.100345.

Data availability

Data will be made available on request.

References

[1] A. Inoue, Stabilization of metallic supercooled liquid and bulk amorphous alloys, Acta Mater. 48 (2000) 279–306, https://doi.org/10.1016/S1359-6454(99)00300-6.
[2] W.H. Wang, C. Dong, C.H. Shek, Bulk metallic glasses, Mater. Sci. Eng. R 44 (2004) 45–89, https://doi.org/10.1016/j.mser.2004.03.001.
[3] I. Gallino, R. Busch, Physical metallurgy of bulk metallic glass-forming liquids: thermodynamic and kinetic concepts in glass formation, in: Springer Series in Materials Science, 341, Springer, Cham, Switzerland, 2024.
[4] W.L. Johnson, Bulk glass-forming metallic alloys: science and technology, MRS Bull. 24 (1999) 42–56, https://doi.org/10.1557/S0883769400053252.
[5] J.J. Kruzic, Bulk metallic glasses as structural materials: a review, Adv. Eng. Mater. 18 (2016) 1308–1331, https://doi.org/10.1002/adem.201600066.
[6] J.F. Löffler, Bulk metallic glasses, Intermetallics 11 (2003) 529–540, https://doi.org/10.1016/S0966-9795(03)00046-3.
[7] P. Tiberto, M. Baricco, E. Olivetti, R. Piccin, Magnetic properties of bulk metallic glasses, Adv. Eng. Mater. 9 (2007) 468–474, https://doi.org/10.1002/adem.200700050.
[8] G. Herzer, Modern soft magnets: amorphous and nanocrystalline materials, Acta Mater. 61 (2013) 718–734, https://doi.org/10.1016/j.actamat.2012.10.040.
[9] C. Suryanarayana, A. Inoue, Iron-based bulk metallic glasses, Int. Mater. Rev. 58 (2013) 131–166, https://doi.org/10.1179/1743280412Y.0000000007.
[10] H.X. Li, Z.C. Lu, S.L. Wang, Y. Wu, Z.P. Lu, Fe-based bulk metallic glasses: glass formation, fabrication, properties and applications, Prog. Mater. Sci. 103 (2019) 235–318, https://doi.org/10.1016/j.pmatsci.2019.01.003.
[11] J.M. Silveyra, E. Ferrara, D.L. Huber, T.C. Monson, Soft magnetic materials for a sustainable and electrified world, Science 362 (2018) eaao0195, https://doi.org/10.1126/science.aao0195.
[12] S. Sohrabi, J. Fu, L. Li, Y. Zhang, X. Li, F. Sun, J. Ma, W.H. Wang, Manufacturing of metallic glass components: processes, structures and properties, Prog. Mater. Sci. 144 (2024) 101283, https://doi.org/10.1016/j.pmatsci.2024.101283.
[13] P. Zhang, J. Tan, Y. Tian, H. Yan, Z. Yu, Research progress on selective laser melting (SLM) of bulk metallic glasses (BMGs): a review, Int. J. Adv. Manuf. Technol. 118 (2021) 2017–2057, https://doi.org/10.1007/s00170-021-07990-8.
[14] C. Zhang, D. Ouyang, S. Pauly, L. Liu, 3D printing of bulk metallic glasses, Mater. Sci. Eng. R 145 (2021) 100625, https://doi.org/10.1016/j.mser.2021.100625.

[15] H.R. Lashgari, M. Ferry, S. Li, Additive manufacturing of bulk metallic glasses: fundamental principle, current/future developments and applications, J. Mater. Sci. Technol. 119 (2022) 131–149, https://doi.org/10.1016/j.jmst.2021.09.068.
[16] N. Sohrabi, J. Jhabvala, R.E. Logé, Additive manufacturing of bulk metallic glasses—process, challenges and properties: a review, Metals 11 (2021) 1279, https://doi.org/10.3390/met11081279.
[17] M.G. Özden, N.A. Morley, Laser additive manufacturing of Fe-based magnetic amorphous alloys, Magnetochmetristry 7 (2021) 20, https://doi.org/10.3390/magnetochemistry7020020.
[18] M. Rodríguez-Sánchez, S. Sadanand, A. Ghavimi, R. Busch, P. Tiberto, E. Ferrara, G. Barrera, L. Thorsson, H.J. Wachter, I. Gallino, M.T. Pérez-Prado, Relating laser powder bed fusion process parameters to (micro)structure and to soft magnetic behaviour in a Fe-based bulk metallic glass, Materialia 35 (2024) 102111, https://doi.org/10.1016/j.mtla.2024.102111.
[19] W. Xing, D. Ouyang, N. Li, L. Liu, Insight into micro-cracking in 3D-printed Fe-based BMGs by selective laser melting, Intermetallics 103 (2018) 101–106, https://doi.org/10.1016/j.intermet.2018.10.011.
[20] N. Li, J. Zhang, W. Xing, D. Ouyang, L. Liu, 3D printing of Fe-based bulk metallic glass composites with combined high strength and fracture toughness, Mater. Des. 143 (2018) 285–296, https://doi.org/10.1016/j.matdes.2018.01.061.
[21] X.D. Nong, X.L. Zhou, Y.X. Ren, Fabrication and characterization of Fe-based metallic glasses by selective laser melting, Opt. Laser. Technol. 109 (2019) 20–26, https://doi.org/10.1016/j.optlastec.2018.07.059.
[22] Ł. Żrodowski, B. Wysocki, R. Wróblewski, A. Krawczyńska, B. Adamczyk-Cieślak, J. Zdunek, P. Błyskun, J. Ferenc, M. Leonowicz, W. Święszkowski, New approach to amorphization of alloys with low glass forming ability via selective laser melting, J. Alloys Compd. 771 (2019) 769–776, https://doi.org/10.1016/j.jallcom.2018.08.075.
[23] Y.G. Nam, B. Koo, M.S. Chang, S. Yang, J. Yu, Y.H. Park, J.W. Jeong, Selective laser melting vitrification of amorphous soft magnetic alloys with help of double-scanning-induced compositional homogeneity, Mater. Lett. 261 (2020) 127068, https://doi.org/10.1016/j.matlet.2019.127068.
[24] L. Thorsson, M. Unosson, M.T. Pérez-Prado, X. Jin, P. Tiberto, G. Barrera, B. Adam, N. Neuber, A. Ghavimi, M. Frey, R. Busch, I. Gallino, Selective laser melting of a Fe-Si-Cr-B-C-based complex-shaped amorphous soft-magnetic electric motor rotor with record dimensions, Mater. Des. 215 (2022) 110483, https://doi.org/10.1016/j.matdes.2022.110483.
[25] M.G. Özden, N.A. Morley, Optimizing laser additive manufacturing process for Fe-based nano-crystalline magnetic materials, J. Alloys Compd. 960 (2023) 170644, https://doi.org/10.1016/j.jallcom.2023.170644.
[26] M.G. Özden, F.S. Freeman, N.A. Morley, Soft-magnetic behavior of Fe-based nanocrystalline alloys produced using laser powder bed fusion, Adv. Eng. Mater. 25 (2023) 2201508, https://doi.org/10.1002/adem.202300597.
[27] M. Rodríguez-Sánchez, A. Boccardo, S. Sadanand, A. Ghavimi, R. Busch, P. Sharangi, E. Ferrara, G. Barrera, P. Tiberto, D. Tourret, I. Gallino, M.T. Pérez-Prado, Laser powder bed fusion of an Fe-based metallic glass using time delays, Addit. Manuf. 110 (2025) 104922, https://doi.org/10.1016/j.addma.2025.104922.
[28] I. Otsuka, K. Wada, Y. Maeta, T. Kadomura, M. Yagi, Magnetic properties of Fe-based amorphous powders with high-saturation induction produced by spinning water atomization process (SWAP), IEEE Trans. Magn. 44 (2008) 3891–3894, https://doi.org/10.1109/TMAG.2008.2002249.
[29] J. Schindelin, I. Arganda-Carreras, E. Frise, V. Kaynig, M. Longair, T. Pietzsch, S. Preibisch, C. Rueden, S. Saalfeld, B. Schmid, J.-Y. Tinevez, D.J. White, V. Hartenstein, K. Eliceiri, P. Tomancak, A. Cardona, Fiji: an open-source platform for biological-image analysis, Nat. Methods 9 (2012) 676–682, https://doi.org/10.1038/nmeth.2019.
[30] I. Arganda-Carreras, V. Kaynig, C. Rueden, K.W. Eliceiri, J. Schindelin, A. Cardona, H.S. Seung, Trainable Weka segmentation: a machine learning tool for microscopy pixel classification, J. Bioinform. 33 (2017) 2424–2426, https://doi.org/10.1093/bioinformatics/btx180.
[31] T. DebRoy, H.L. Wei, J.S. Zuback, T. Mukherjee, J.W. Elmer, J.O. Milewski, A. M. Beese, A. Wilson-Heid, A. De, W. Zhang, Additive manufacturing of metallic components – process, structure and properties, Prog. Mater. Sci. 92 (2018) 112–224, https://doi.org/10.1016/j.pmatsci.2017.10.001.
[32] S.Y. Ahn, S.G. Jeong, M.J. SaGong, G. Lee, E.S. Kim, H. Park, J.W. Cho, J.G. Kim, H. S. Kim, Size matters: exploring part size effects on microstructure, defects, and mechanical property in optimized laser powder bed fusion (L-PBF) additive manufacturing, Mater. Sci. Eng. A 902 (2024) 146616, https://doi.org/10.1016/j.msea.2024.146616.
[33] I. Rodríguez-Barber, A.M. Fernández-Blanco, I. Unanue-Arruti, I. Madariaga-Rodríguez, S. Milenkovic, M.T. Pérez-Prado, Precontouring as a tool to improve the laser powder bed fusion printability of Inconel 939 thin walls, Adv. Eng. Mater. 27 (2025) 2401929, https://doi.org/10.1002/adem.202401929.
[34] N. Sohrabi, T. Ivas, J. Jhabvala, J.E. Schawe, J.F. Löffler, H. Ghasemi-Tabasi, R. E. Logé, Quantitative prediction of crystallization in laser powder bed fusion of a Zr-based bulk metallic glass with high oxygen content, Mater. Des. 239 (2024) 112744, https://doi.org/10.1016/j.matdes.2024.112744.
[35] S.I. Shahabad, U. Ali, Z. Zhang, A. Keshavarzkermani, R. Esmaeilizadeh, A. Bonakdar, E. Toyserkani, On the effect of thin-wall thickness on melt pool dimensions in laser powder-bed fusion of Hastelloy X: numerical modeling and experimental validation, J. Manuf. Process. 75 (2022) 435–449, https://doi.org/10.1016/j.jmapro.2022.01.029.
[36] Y. Sun, H. Zhao, R. Huang, L. Liu, C. Tan, D. Lin, B. Chen, X. Song, R. Ma, The effect of thickness on the defects and anisotropy of thin-wall Hastelloy X fabricated via laser powder-bed fusion, J. Mater. Res. Technol. 27 (2023) 703–717, https://doi.org/10.1016/j.jmrt.2023.10.025.
[37] S. Chowdhury, N. Yadaiah, C. Prakash, S. Ramakrishna, S. Dixit, L.R. Gupta, D. Buddhi, Laser powder bed fusion: a state-of-the-art review of the technology, materials, properties & defects, and numerical modelling, J. Mater. Res. Technol. 20 (2022) 2109–2172, https://doi.org/10.1016/j.jmrt.2022.07.121.
[38] H.Y. Jung, S.J. Choi, K.G. Prashanth, M. Stoica, S. Scudino, S. Yi, U. Kühn, D. H. Kim, K.B. Kim, J. Eckert, Fabrication of Fe-based bulk metallic glass by selective laser melting: a parameter study, Mater. Des. 86 (2015) 703–708, https://doi.org/10.1016/j.matdes.2015.07.145.
[39] D. Ouyang, W. Xing, N. Li, Y. Li, L. Liu, Structural evolutions in 3D-printed Fe-based metallic glass fabricated by selective laser melting, Addit. Manuf. 23 (2018) 246–252, https://doi.org/10.1016/j.addma.2018.08.020.
[40] A.L. Greer, M.B. Costa, O.S. Houghton, Metallic glasses, MRS Bull. 48 (2023) 1054–1061, https://doi.org/10.1557/s43577-023-00586-5.
[41] C.A. Schuh, T.C. Hufnagel, U. Ramamurty, Mechanical behavior of amorphous alloys, Acta Mater. 55 (2007) 4067–4109, https://doi.org/10.1016/j.actamat.2007.01.052.
[42] J. Shi, S. Ma, S. Wei, J.P. Best, M. Stolpe, B. Markert, Connecting structural defects to tensile failure in a 3D-printed fully-amorphous bulk metallic glass, Mater. Sci. Eng. A 813 (2021) 141106, https://doi.org/10.1016/j.msea.2021.141106.
[43] R. Spatschek, C. Gugenberger, E. Brener, Effective elastic moduli in solids with high crack density, Phys. Rev. B 80 (2009) 144106, https://doi.org/10.1103/PhysRevB.80.144106.
[44] Y. Murakami, N.Z. Gakkai, Stress Intensity Factors Handbook, 3, Society of Materials Science, Japan, 1992.
[45] P. Agarwal, D. Mathur, S.S. Ghosh, Formulation of stress concentration factor of a finite plate with an elliptical hole of high eccentricity ratio, in: A. Parey, R. Kumar, M. Singh (Eds.), Recent Trends in Engineering Design. Lecture Notes in Mechanical Engineering, Springer, Singapore, 2021.
[46] S. Sadanand, M. Rodríguez-Sánchez, A. Ghavimi, R. Busch, P. Sharangi, P. M. Tiberto, E. Ferrara, G. Barrera, L. Thorsson, H.J. Wachter, I. Gallino, M.T. Pérez-Prado, Laser powder bed fusion of a nanocrystalline Finemet Fe-based alloy for soft magnetic applications, J. Laser Appl. 36 (2024) 042029, https://doi.org/10.2351/7.0001391.
[47] P. Novák, E. Duchková, A. Boháčová, A. Michalcová, F. Průša, K. Skotnicová, I. Szurman, Synthesis and properties of iron silicides, J. Mater. Res. Technol. 38 (2025) 165–174, https://doi.org/10.1016/j.jmrt.2025.07.129.
[48] J. Lentz, A. Röttger, W. Theisen, Hardness and modulus of Fe_2B, $Fe_3(C,B)$, and $Fe_{23}(C,B)_6$ borides and carboborides in the Fe–C–B system, Mater. Charact. 135 (2018) 192–202, https://doi.org/10.1016/j.matchar.2017.11.012.